

Internal dynamics of Newtonian and viscoplastic fluid avalanches down a sloping bed

Nicolas Andreini, Gaël Epely-Chauvin, and Christophe Ancey

École Polytechnique Fédérale de Lausanne, Écublens, 1015 Lausanne, Switzerland

(Received 9 August 2011; accepted 30 April 2012; published online 14 May 2012)

We experimentally investigated the spreading of fluid avalanches (i.e., fixed volumes of fluid) down an inclined flume. Emphasis was given to the velocity field within the head. Using specific imaging techniques, we were able to measure velocity profiles within the flowing fluid far from the sidewalls. We studied the behavior of Newtonian and viscoplastic fluids for various flume inclinations and initial masses. For the Newtonian fluids tested (glycerol and Triton X100), we compared the measured velocity field with that predicted by lubrication theory. Provided that the flow Reynolds number Re was sufficiently low (typically $Re < 1$), there was excellent agreement between theory and experiment except for the very thin region just behind the contact line. For higher Reynolds numbers (typically $Re \sim 10$), the discrepancy between theory and experiment was more marked (relative errors up to 17% for the body). As viscoplastic materials, we used Carbopol ultrez 10. For the body, agreement between theoretical and measured velocity profiles was fairly satisfactory whereas it was very poor for the tip region as the curvature of the free surface became more pronounced: the velocities were not only much lower than those predicted by lubrication theory, but there was also evidence of slipping in the flow part adjacent to the contact line.

© 2012 American Institute of Physics. [<http://dx.doi.org/10.1063/1.4718018>]

I. INTRODUCTION

In this paper, we report new experimental results that characterize the dynamics of fluid avalanches down a sloping bed. More particularly, we focus on the velocity field within the head of thin elongated flows for two rheologies: Newtonian fluids (glycerol, Triton) and a viscoplastic polymeric gel (Carbopol ultrez 10).

The flow of a fixed volume of fluid down an inclined surface has attracted considerable attention over the last decades. In terms of applications, this problem is of particular relevance to industrial flows, e.g., coating films,^{1,2} design of consistometer in food industry.³⁻⁵ In geophysical fluid mechanics, the Newtonian and viscoplastic models have often been used as a first approximation to the rheological behavior of complex slurries: debris flows, tailings dams, lava flows, and snow avalanches.⁶⁻¹⁰ The Newtonian case is also regarded as a limiting case of (starving) gravity currents and has been studied in lock-exchange problems under laminar flow conditions.^{11,12} From the fundamental standpoint, there has been continuing interest in the development of a compact set of equations that can describe the motion of finite volumes of fluid along a horizontal surface or down an inclined plane. Indeed, in addition to its practical significance, this flow configuration raises a number of questions as regards flow unsteadiness, front dynamics (contact line, stability, and fingering), time-dependent free surface (shape and wave pattern), balance between two or more processes (gravity acceleration, viscous dissipation, inertia, and pressure gradient), and the approach to an asymptotic steady state or arrested state. Two approaches have emerged for deriving the governing equations: one is the integral (Saint-Venant) approach that consists of taking the depth average of the local (Cauchy) equations,^{7,13-16} while the second is lubrication theory, which exploits the flow shallowness to simplify the local governing equations.¹⁷⁻²⁷ Some of the assumptions underpinning the derivation of the governing equations (e.g., the expression of the source term in the momentum balance equation or the existence of true plug flows) are still vividly debated.^{13,16,21}

Surprisingly enough, in spite of this considerable interest, there are few comprehensive experimental investigations of time-dependent flows involving a Newtonian or viscoplastic fluid over a solid boundary and most of them focus on macroscopic features such as the flow depth profiles or the front position as a function of time.^{7,17,25,26,28–30} In this paper, we provide further insight into the dynamics of the head of Newtonian and viscoplastic flows not only by tracking the shape evolution but also by measuring the velocity field inside the flow and far from the sidewalls. To that end, an innovative combination of imaging techniques has been used. The paper is organized as follows. First, we will outline the theoretical background. Then, we will present the experimental data for the Newtonian fluids. Finally, we will provide a few results obtained with viscoplastic fluids. The Appendix provides further information on the theoretical framework (integral formulation and dimensionless numbers) together with numerical and analytical solutions to the dam break problem for viscous fluids.

II. THEORY

A. Viscous theory

Let us consider a thin layer of fluid released from a reservoir and flowing down a plane inclined at an angle θ to the horizontal (see Fig. 1). The fluid is Newtonian with viscosity μ and density ρ . The initial volume is V . We define a two-dimensional Cartesian coordinate system in which the x axis points down the flume, the y axis is in the direction of the upward pointing normal. The rear end of the reservoir is chosen to be the origin of the x axis. The bulk velocity \mathbf{u} has components u and v in each of these directions, respectively. The flow depth is denoted by $h(x, t)$.

In the following treatment, we assume that the characteristic lengthscale along the bed is much greater than the typical layer thickness. Assuming that the fluid moves slowly, we can neglect the inertial terms in the Navier-Stokes equations. Surface tension is also neglected. The shallowness assumption is the cornerstone that underpins lubrication theory and makes it possible to simplify a great deal the governing equations (the Navier-Stokes equations). Using dimensional analysis and asymptotic expansions (see the Appendix), it is possible to derive several regimes and describe their flow properties.^{26,31} Here, for the sake of simplicity, we skip many of the mathematical details to focus on the physical meaning of the solution (from the mathematical standpoint, much more attention must be paid to justifying the asymptotic expansions that underpin the results presented thereafter²⁶). The shallow flow approximation leads to a hydrostatic distribution of the fluid pressure

$$p = \rho g \cos \theta (h - y), \quad (1)$$

while the streamwise velocity component is given by the momentum balance equation

$$\frac{\partial \tau}{\partial y} + \rho g \sin \theta = \rho g \cos \theta \frac{\partial h}{\partial x}, \quad (2)$$

with $\tau = \mu \dot{\gamma}$ denoting the shear stress ($\dot{\gamma} = du/dy$ is the shear rate). Integrating Eq. (2) shows that the velocity profile takes a parabolic shape, whose amplitude is modulated by the free

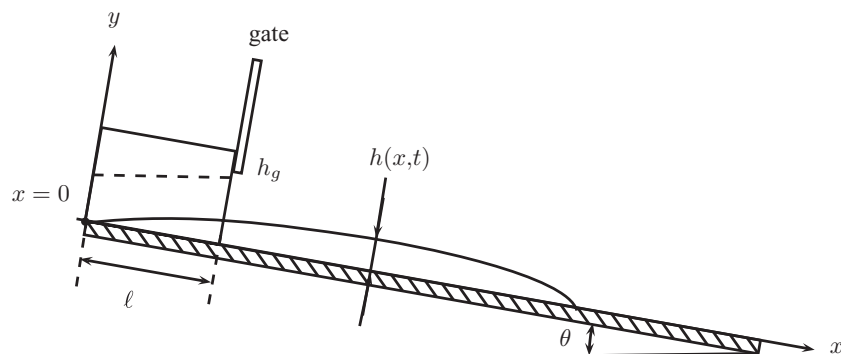


FIG. 1. Sketch defining the flow configuration.

surface curvature

$$u(x, y, t) = \frac{1}{2}Ky(2h - y) \left(1 - \cot\theta \frac{\partial h}{\partial x}\right) \text{ with } K = \frac{\rho g \sin\theta}{\mu}. \quad (3)$$

The continuity equation yields the normal velocity profile

$$v(x, y, t) = \frac{1}{2}Ky^2 \left(\frac{\partial h}{\partial x} \left(1 - \cot\theta \frac{\partial h}{\partial x}\right) - \frac{\partial^2 h}{\partial x^2} \left(1 - \frac{y}{3}\right) \cot\theta\right). \quad (4)$$

A new integration of Eq. (3) leads to the depth-averaged velocity

$$\bar{u}(x, t) = \frac{1}{h} \int_0^h u(x, y, t) dy = \frac{1}{3}Kh^2 \left(1 - \cot\theta \frac{\partial h}{\partial x}\right). \quad (5)$$

Conservation of mass leads to the governing equation for the flow depth $h(x, t)$, which is a nonlinear advection-diffusion equation

$$\frac{\partial h}{\partial t} + Kh^2 \frac{\partial h}{\partial x} = Kh^2 \cot\theta \left(\frac{\partial h}{\partial x}\right)^2 + \frac{Kh^3}{3} \cot\theta \frac{\partial^2 h}{\partial x^2}. \quad (6)$$

The only exact solutions available are for horizontal bottoms ($\theta = 0$), for which the governing equation reduces to a nonlinear diffusion equation.^{19,32} Asymptotic solutions can be obtained at short and long times.^{17,18,26} For instance, it can be shown that at sufficiently long times, the spread of a finite volume V on a horizontal surface is given by

$$x_f(t) = \xi_f \left(\frac{\rho g V^3}{3\mu} t\right)^{1/5}, \quad (7)$$

with $\xi_f = 1.411$, while the front position of a fluid avalanche over a tilted plane is approximated by the first-order expression

$$x_f(t) = \left(\frac{9}{4} \frac{\rho g \sin\theta V^2}{\mu} t\right)^{1/3}. \quad (8)$$

B. Viscoplastic theory

Lubrication theory can also be applied to viscoplastic flows.^{20,21,23,25,27} Here, we consider viscoplastic fluids whose behavior can be described using the empirical Herschel-Bulkley law. For simple shear flow, this law implies that there is motion only when the shear stress τ exceeds a threshold called the yield stress τ_c

$$\kappa \dot{\gamma}^n = \begin{cases} \tau - \tau_c & \text{for } \tau > \tau_c, \\ 0 & \text{for } \tau \leq \tau_c, \end{cases} \quad (9)$$

where n is called the shear thinning index (in most cases $n \leq 1$) and κ is the consistency. After substituting τ by the constitutive relation (9) into the momentum balance equation (2) and integrating it, we readily obtain the velocity profile

$$u(x, y, t) = \begin{cases} \frac{n}{n+1} \hat{K}^{1/n} \left(Y_0^{1+1/n} - (Y_0 - y)^{1+1/n}\right) \left(1 - \cot\theta \frac{\partial h}{\partial x}\right)^{1/n} & \text{for } y \leq Y_0, \\ \frac{n}{n+1} \hat{K}^{1/n} \left(1 - \cot\theta \frac{\partial h}{\partial x}\right)^{1/n} Y_0^{1+1/n} & \text{for } y > Y_0, \end{cases} \quad (10)$$

with $\hat{K} = \rho g \sin\theta / \kappa$ and where $Y_0 = \max(0, h - \tau_c / (\rho g \cos\theta (\tan\theta - \partial_x h)))$ denotes the position of the interface between the sheared and unsheared layers; it is called the *yield surface*. The nature of the unsheared layer (also called the *plug*) in an elongating flow has been widely debated: questioning the existence of a plug layer within the tip region, Piau¹³ suggested that the entire layer should be sheared. Taking a closer look at the matched asymptotic expansions used to derive the governing equations, Balmforth and Craster²¹ have shown that the plug region is in fact slightly sheared and for this reason, should be better referred to as the *pseudo-plug layer*, and the yield surface as the *pseudo-yield surface*.

III. EXPERIMENTAL FACILITY AND PROCEDURE

A. Fluids

As Newtonian fluids, we used three liquids: 98.5% glycerol solution (density $\rho = 1260 \text{ kg m}^{-3}$, viscosity $\mu = 1110 \text{ mPa s}$ at a temperature of $20 \text{ }^\circ\text{C}$), pure glycerol (density $\rho = 1260 \text{ kg m}^{-3}$, viscosity $\mu = 1490 \text{ mPa s}$ at a temperature of $20 \text{ }^\circ\text{C}$), both manufactured by Reactolab (Switzerland), and Triton X100 (density $\rho = 1067 \text{ kg m}^{-3}$, viscosity $\mu = 468 \text{ mPa s}$ at a temperature of $20 \text{ }^\circ\text{C}$) produced by Interchim Bioscience (Switzerland). Viscosity was measured using a Bohlin CVOR rheometer equipped with a cone and plate geometry; density was measured using an aerometer to within 1%. The refractive index n_r was 1.4730 for glycerol (98.5% solution) and 1.49171 for Triton. Surface tension was measured using the pendant drop test (with a 0.74-mm wide needle) and image processing.³³ We found $\sigma = 51 \text{ mN m}^{-1}$ for glycerol and $\sigma = 32 \text{ mN m}^{-1}$ for Triton X100 (measurement uncertainty as high as 20%).

As glycerol absorbed water vapor, it was very difficult to use pure glycerol and for that reason, most runs were done with the 98.5% glycerol solution. Note that Triton is not a genuinely Newtonian fluid. It was slightly shear thinning, with a flow curve closely approximated by a power law function

$$\tau = \kappa \dot{\gamma}^n, \quad (11)$$

with $n = 0.935$ the shear-thinning index and $\kappa = 0.481 \text{ Pa s}^{-n}$ (at $20 \text{ }^\circ\text{C}$) the effective viscosity. Moreover, as the dynamic viscosity was highly sensitive to temperature changes (typically increasing the temperature by $1 \text{ }^\circ\text{C}$ caused the viscosity to decrease by about 35 mPa s for Triton and about 65 mPa s for glycerol), all the experiments were carried out under controlled temperature conditions (at $20.0 \pm 0.1 \text{ }^\circ\text{C}$).

As viscoplastic fluids, we used Carbopol ultrez 10 (we also tested ultrez 21) at a mass concentration of 0.15%. Given the low concentration in Carbopol, the density and refractive index are those of water: $\rho = 1000 \text{ kg m}^{-3}$ and $n_r = 1333$. The sample was prepared as follows: the Carbopol powder was gently poured and dispersed in a large volume of demineralized water heated at $55 \text{ }^\circ\text{C}$. The dispersion was left at rest for a few hours (typically one night). The pH was adjusted to 7.70 ± 0.05 by adding a sodium hydroxide solution. After mixing the sample vigorously, we added a tiny amount of polyamid particles (for particle image velocimetry (PIV) measurements). To ensure homogeneity and remove gas bubbles trapped during the previous phases, we mixed the sample very slowly (4 rpm) for 12 h. We measured the rheological properties using a parallel plate geometry (with serrated plates, diameter 60 mm, and gap 2 mm) mounted on a Bohlin CVOR rheometer. Serrated surfaces were needed to avoid/limit wall slip. On average, we had: $\tau_c = 33 \text{ Pa}$, $n = 0.33$, and $\kappa = 26 \text{ Pa s}^n$. Reproducibility tests carried out with other geometries showed that the uncertainty on the rheological parameters was more significant than for the Newtonian liquids. We estimated that the maximum deviation was $\Delta\tau_c = 2 \text{ Pa}$ (relative uncertainty 6%), $\Delta n = 0.02$ (relative uncertainty 6%), and $\Delta\kappa = 4 \text{ Pa s}^n$ (relative uncertainty 15%). Additional tests showed that Carbopol ultrez 10 was negligibly viscoelastic and thixotropic.

All our fluids were seeded with polyamid particles for particle imaging velocimetry. The particles (polyamide 12 particles manufactured by Dantec Dynamics, mean diameter $20 \text{ } \mu\text{m}$, density 1030 kg m^{-3}) were marked with rhodamine by leaving them in a concentrated rhodamine solution (maintained at $60 \text{ }^\circ\text{C}$) for one month. They were then rinsed with alcohol several times to avoid subsequent contamination of the samples by rhodamine. Note that the density mismatch between the PIV particles and the carrier fluid had negligible effects as the settling velocity (approximately $0.05 \text{ } \mu\text{m s}^{-1}$) was very low compared to the streamwise velocity (approximately 10 cm s^{-1}). We also suspected rhodamine to have an effect on Carbopol on the long term and for this reason, Carbopol samples were used quickly after their preparation (after PIV particles were added).

B. Flume

Experiments were conducted in a flume with a transparent bottom (PMMA plate, refractive index $n_r = 1.488$). The flume was 3.5 m long and 10 cm wide. It could be inclined from 0° to 35° . Its position was accurately controlled using a digital inclinometer with a precision of 0.1° . The

upper part of flume was equipped with a sluice gate mounted on a pneumatic jack and was used as a reservoir. The jack was quickly raised by injecting air pressured at 7 MPa, which made it possible to lift the gate within 0.5 s. Recall that we defined a two-dimensional Cartesian coordinate system in which the x axis points down the flume, the y axis is in the direction of the upward pointing normal, and the z axis is the cross-stream direction (see Fig. 1). The upper end of the flume is at $x = 0$, while the lower end is at $x = 350$ cm. $z = 0$ refers to the right sidewall (when looking at the flume from the inlet), while $z = W = 10$ cm refers to the left sidewall.

C. Measurement systems

We took the following measurements: (i) the velocity field in a vertical plane Oxy passing through the centerline of the flume ($z = 5$ cm) and normal to the flume bottom and (ii) the position of the front as a function of time. To that end, we used a dual head, diode pumped, Q-switched Nd:YLF Laser (Litron LDY 303). The laser had two optical cavities emitting a 527-nm beam (green), with energy up to 20 mJ per pulse at 1 kHz. Velocities were measured using high-speed cameras and PIV techniques. For PIV measurements, we used a Basler A504k camera (working in the 200–1000 Hz range), mounted with a Nikkor 105 mm macrolens and an orange filter. The images were then processed using classic PIV techniques.³⁴ Velocity fields were computed using the open source software called MatPIV.³⁵ Front position was monitored using two Basler A403kc cameras.

Figure 2 explains how we measured the velocity profiles from below using the Scheimpflug principle (see Fig. 2 and, e.g., see Chap. 7 in Raffel *et al.*³⁴ for additional information). Filming from the side did not make it possible to measure velocities within the head far from the sidewall owing to the strong curvature (in both x - and z axis) and flow shallowness of the front. On the contrary, filming from below gave direct optical access to the vertical plane passing through the centerline, but

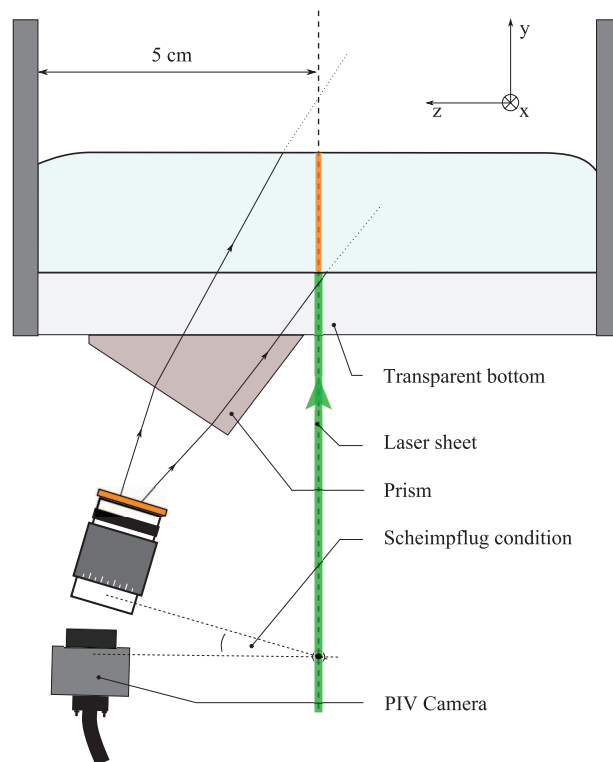


FIG. 2. Sketch of the measurement system for the velocity profiles within the moving fluid. Because of the fluid/air interface and the three-dimensional nature of the flows, we were forced to film the flow from below. When shooting images with a camera whose sensor (CCD) is not parallel with the object, one can use the Scheimpflug principle, which involves tilting the camera until the image plane (on the CCD), the lens plane, and the object plane (lit by the laser sheet) have a common line of intersection.

the disadvantage of this configuration was that the largest part of the filmed plane was out of focus. To get around this problem, we adjusted the inclinations of the camera CCD and the lens so that the Scheimpflug rule was satisfied (the image was then in focus). A prism (made up of a PMMA block, with the same refractive index as that of the flume bottom) was also needed to avoid refraction. For Newtonian liquids presented here, slight refraction was induced by the change in the refractive index change at the bottom, but it had negligible effects; refraction was more pronounced for Carbopol. As this system caused significant image distortion, we had to correct it to properly compute the velocity field; this was done by taking a shot of a test chart and using the MATLAB built-in function `cp2tform` to undistort the images.

IV. EXPERIMENTAL RESULTS FOR NEWTONIAN FLUIDS

Table I summarizes the different runs presented in this paper. As bed inclination had direct influence on flow velocity, this was the main parameter we altered to explore the dynamical features of fluid avalanches under different flow conditions. In earlier papers,^{25,26} we reported how the front position and flow depth profiles evolved for highly viscous fluids (concentrated glucose solutions $\mu = 345$ Pa s) and we compared the data with lubrication theory. Here, we will mainly focus on the velocity field inside the flowing material. Yet, to see how well lubrication theory performs as regards the computation of the front position (see Sec. II A), we will first plot the front position as a function of time in a dimensionless form in Fig. 3 and briefly comment on the results.

The measured positions $x_f(t)$ were scaled by the asymptotic values in the form $(Mt)^a$ given by Eq. (7) ($a = 1/5$) for horizontal bottoms and Eq. (8) for sloping flumes ($a = 1/3$). If the scalings (7) and (8) gave fair predictions of the front position, the scaled ratio should tend to unity at sufficiently long times. Since convergence to the asymptotic (similarity) solution could be quite slow,²² we also estimated the time needed to observe the front position lying in a given neighborhood of the asymptotic solution. To that end, we solved the integral equations (Saint Venant) corresponding to our initial boundary value problem using the CLAWPACK library³⁶ (see the Appendix). We then computed the times $t_c^{5\%}$ and $t_c^{10\%}$, from which the deviation between the computed and asymptotic positions of the front dropped below 5% and 10%, respectively. For some simulations [runs (g) and (h)], it was impossible to observe strict convergence for our simulations of flows down a 3.5-m long flume. When we compare the run duration t_e and the convergence times $t_c^{5\%}$ or $t_c^{10\%}$, it turns out that for all runs except for runs (b), (g), and (h), the experimental time should have been sufficiently long to observe relative deviations lower than 5%; for run (b), the relative deviation should lie within the 5%–10% range. For run (g), the numerical simulations showed that the $t^{1/3}$ scaling in Eq. (8) was correct, but the front position was systematically 25% ahead of the asymptotic value given by Eq. (8).

TABLE I. Features of the 8 runs: fluid used, density ρ , dynamic viscosity μ , flume inclination θ , initial mass m , duration of the experiment t_e (time needed for the mass to travel the length between the lock gate and the flume outlet), numerically estimated times of convergence $t_c^{5\%}$ and $t_c^{10\%}$, time t_f (see thereafter), and flow Reynolds number $Re = \rho \bar{u} h / \mu$, where \bar{u} and h denote the depth-averaged velocity and flow depth measured within the body, respectively. We reported the numerical estimates of the times required to observe convergence to the asymptotic solution to within 5% and 10%. t_f denotes the time at which the front reached the position $x = 255$ cm, at which the velocity field was measured.

Run	Fluid	ρ (kg m ⁻³)	μ (mPa s)	θ (deg)	m (kg)	t_e (s)	$t_c^{10\%}$ (s)	$t_c^{5\%}$ (s)	t_f (s)	Re
(a)	98.5% glycerol	1260	1110	0	6	117	1.1	8	61.5	0.08
(b)	98.5% glycerol	1260	1110	1	6	34.2	7	92	24.2	0.40
(c)	98.5% glycerol	1260	1110	3	6	19.2	1.4	1.8	12.6	1.55
(d)	98.5% glycerol	1260	1110	6	6	8.4	1.8	2.6	5.86	6.70
(e)	98.5% glycerol	1260	1110	9	6	5.5	2.1	2.7	3.95	9.33
(f)	98.5% glycerol	1260	1110	6	3	22.9	1.7	7	15.3	1.13
(g)	Pure glycerol	1260	1490	25	1	35.6	21.7	0.27
(h)	Triton X100	1067	468	6	3	8.1	100	...	5.55	9.11

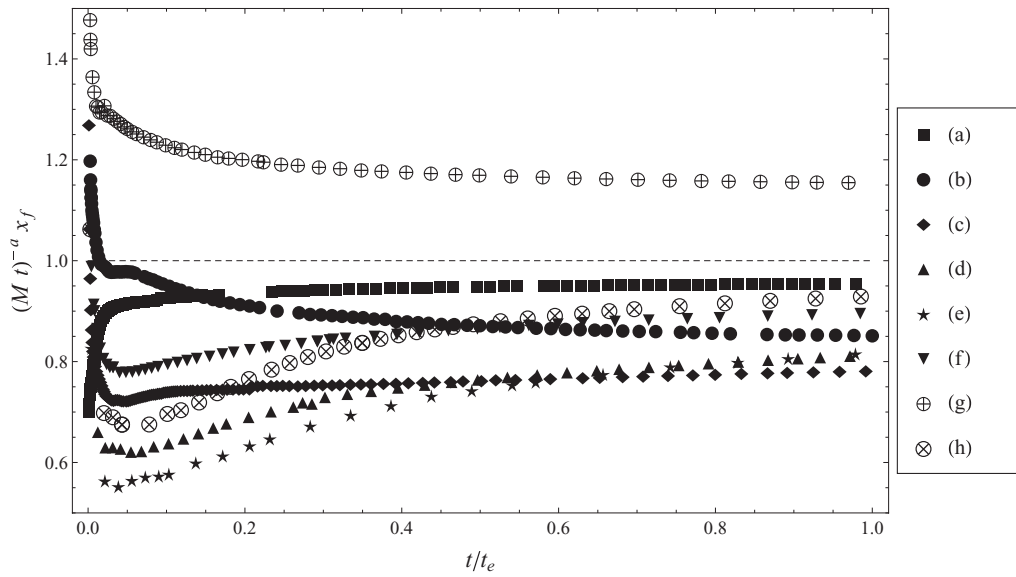


FIG. 3. Variation in the scaled front position with dimensionless time for runs (a)–(h). The front position is made dimensionless by dividing $x_f(t)$ by $(Mt)^a$ with $a = 1/3$ and $M = 9\rho g \sin \theta V^2 / (4\mu)$ for $\theta > 0$ and $a = 1/5$ and $M = 5.59\rho g V^3 / (3\mu)$ for $\theta = 0$. Time t_e is the experiment duration (see Table I). The horizontal dashed line is the asymptotic value to which the scaled front position should tend.

Figure 3 shows that there was an asymptotic value to which the scaled front position tended, but this value significantly differed from unity. For flows involving large masses (6 kg) at the steepest slopes, the asymptotic value was close to 0.8, whereas for the flows at shallow slopes, this value was closer to 0.9. Except for run (g) done at $\theta = 25^\circ$, all measured front positions were lower than the predicted positions. In our earlier experiments done with glucose and a wide flume (30 cm), we also observed a systematic deviation between the theoretical scaling and the measured trend. We primarily thought that there was a delay resulting from the uplift of part of the fluid when we removed the lock gate. However, sidewall friction seems to provide a better explanation for most cases. Indeed, as shown in the Appendix (see Fig. 14), including an empirical correcting factor accounting for sidewall friction reduces significantly the deviations between theory and experimental data. This point deserves further work.

In the rest of this section, we will take a closer look at the velocity profiles inside the flow. We will report both the measured velocity profiles taken in different places (along the centerline) and the theoretical profiles yielded by Eq. (3). Note that making use of this expression requires an equation specifying the gradient of the free surface $\partial_x h(x, t)$. We evaluated $\partial_x h(x, t)$ experimentally by interpolating the measured flow depths by a piecewise linear function: the slope of each segment gave a fairly good local estimate of $\partial_x h(x, t)$. The depth and velocity profiles are plotted relative to the front position ($\Delta x = x - x_f$ is the distance to the front). In all our experiments, we started probing the velocities when the front position was $x_f = 255$ cm.

A. Slope influence

Figure 4 shows the measured and theoretical velocity profiles for runs (a)–(c) pertaining to flows at shallow slopes ($\theta \leq 3^\circ$). Note that only a few datasets have been reported for clarity. We also plotted the flow depth profiles. Remarkably, increasing the bed slope by 3° changed the velocity by a factor 10. For the body and the upper part of the tip region ($x - x_f \geq 10$ cm), there was a fairly good agreement between the theoretical and experimental profiles (with a maximum relative error of 10%). Within the head ($x - x_f \leq 10$ cm), the experimental profiles still kept a parabolic shape, but the velocities were substantially lower than those predicted by Eq. (3). The shallower the slope was, the more pronounced the deviation was. For $\theta = 0$, the relative error was as large as 340% (the

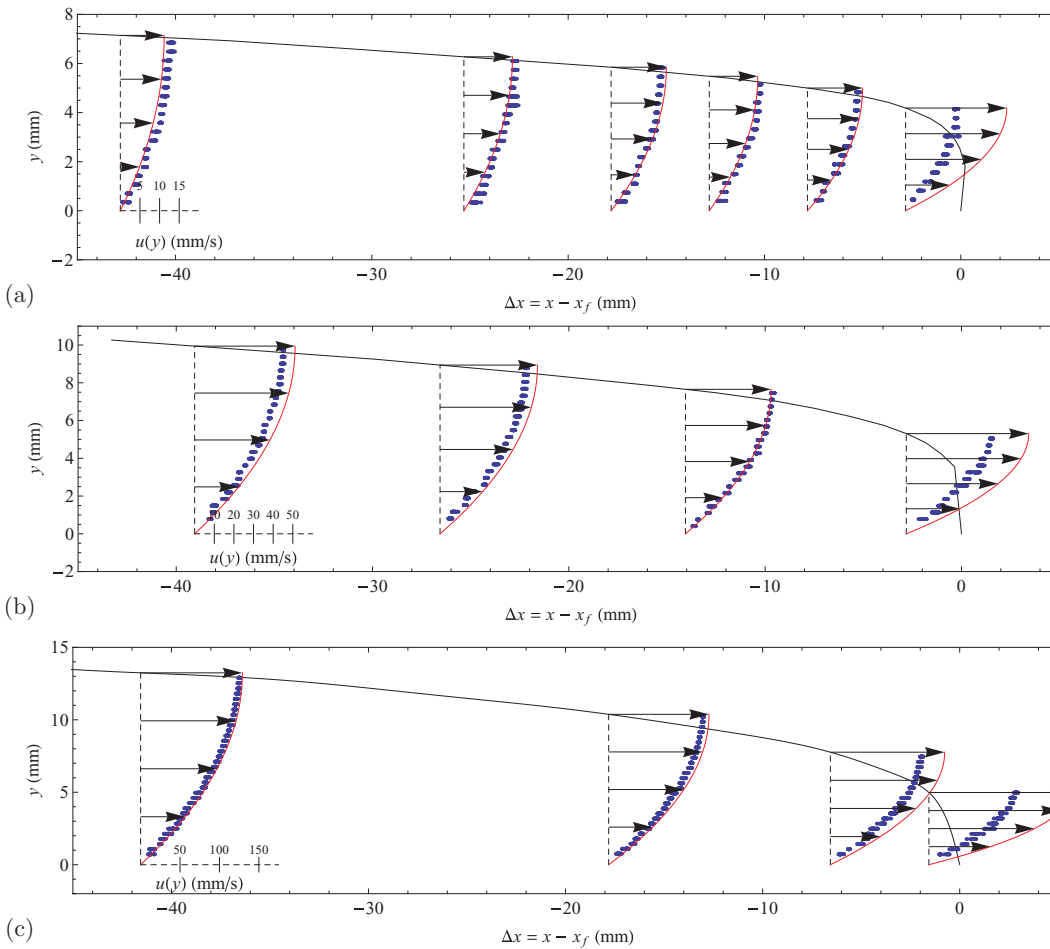


FIG. 4. Velocity profiles for glycerol flows at the shallowest slopes: (a) $\theta = 0^\circ$ [run (a)]; (b) $\theta = 1^\circ$ [run (b)]; (c) $\theta = 3^\circ$ [run (c)]. Initial mass released: 6 kg. The dots represent the measurements, while the solid lines stand for the theoretical profiles provided by Eq. (3).

corresponding data are not shown to keep a reasonable plot range), whereas for $\theta = 3^\circ$, it dropped to 30%.

Figure 5 shows the measured and theoretical velocity profiles for runs (d) and (e) corresponding to flume inclinations $\theta = 6^\circ$ and $\theta = 9^\circ$, respectively. Some changes in the velocity behavior were conspicuous. First, for $\theta = 6^\circ$, the velocity field given by Eq. (3) closely matched the measured velocity profiles even within the head; the maximum relative error was 15%. Then, for $\theta = 9^\circ$, deviations from the expected theoretical profiles were noticeable in the body: at $x - x_f = -65$ mm, the relative deviation was as high as 17%; when approaching the front, the deviation increased and became larger than 50% in the close vicinity of the contact line. Since this flow was characterized by the highest Reynolds number ($Re \sim 9.33$ in the body), one reasonable explanation for the systematic discrepancy between the predicted velocity profiles and the measurements stems from the development of inertial effects.

Surprisingly enough, the measured velocities were higher than the predicted velocities for the body and upper part of the head ($x - x_f \leq -1.6$ mm). Computation of the mass flux $h\bar{u}$ showed that for the experiments at the shallowest slopes ($\theta \leq 3^\circ$), it was increasing with distance (i.e., the mass flux was larger in the body than that in the vicinity of the contact line) as was expected theoretically, whereas at steeper slopes, it remained nearly constant (except near the contact line, where it dropped abruptly). This suggests there must be flow recirculation within the tip region to allow for the constant mass flux in the x-direction. Consistently with the analytical calculations of the velocity

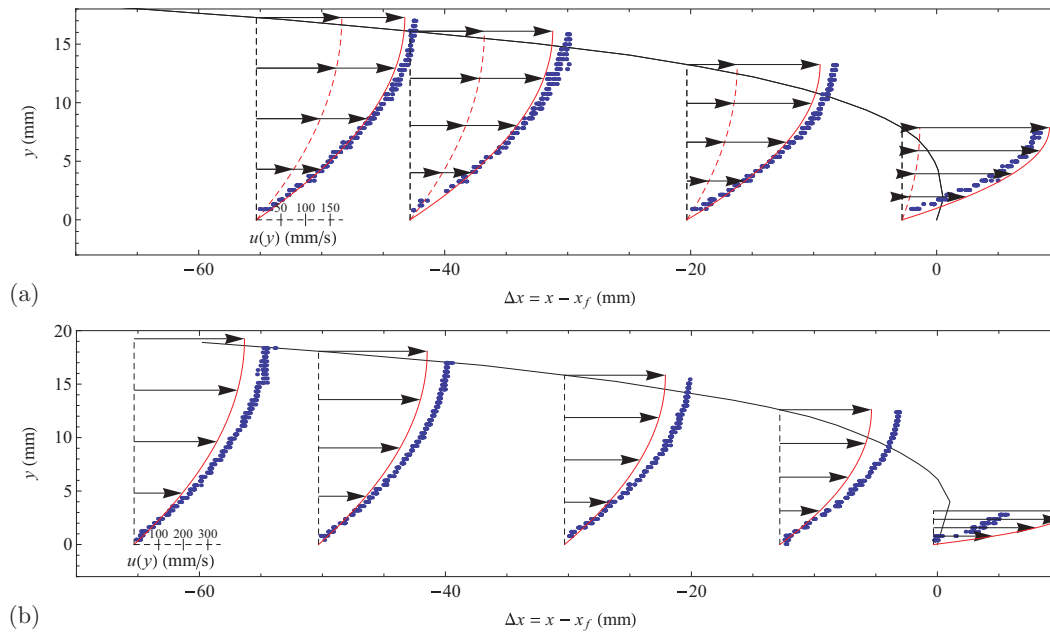


FIG. 5. Velocity profiles for glycerol flows at steeper slopes: (a) $\theta = 6^\circ$ [run (d)]; (b) $\theta = 9^\circ$ [run (e)]. Initial mass released: 6 kg. The dots represent the measurements, while the solid lines stand for the theoretical profiles provided by Eq. (3). For run (d), the dashed lines represent the velocity profiles in a steady uniform regime, i.e., by setting the depth gradient term to zero in Eq. (3).

field within an intrusive front between parallel plates,³⁷ this recirculation might have been created by a pair of counter-rotating vortices within the tip region, on either side of the centerline, and with axis of rotation normal to the flume bottom: fluid parcels were sucked toward the centerline, which contributed to increase the mass balance and give a blunter shape to the contact line, as shown in Fig. 6. This is a speculative explanation, which does not rely on measurements (which would have been difficult to take within the moving head with sufficient accuracy).

To illustrate the importance of the depth gradient in the velocity computation, we have plotted the velocity profiles pertaining to the steady uniform flow on Fig. 5(a). These profiles were readily obtained by setting $\partial_x h = 0$ in Eq. (3). They significantly differed from the measured velocities: for $\Delta x \sim -60$ mm (somewhere in between the contact line and the body), the relative error was as large as 50%, while it exceeded 90% nearby the contact line. This result may seem intriguing in that in analytical calculations of the front position as a function of time^{7,17,18,26} (see the Appendix), it is assumed that the depth-averaged velocity accommodates with any local change in the flow depth as if the flow were at equilibrium, i.e., steady and uniform. This assumption allows to simplifying a great deal the governing equation (6), which then reduces to a simple nonlinear advection equation; in this case, the spreading rate is given by the relation (8), which is considered to provide the correct scaling of the front position with time.

B. Mass influence

Figure 7(a) shows the velocity profiles for a mass of 3 kg down a flume inclined at 6° . Figure 7(b) shows the profiles of the normal velocity component $v(x, y, t)$. This velocity component was of low amplitude (typically 2 mm/s for the body) compared to the streamwise component u even in the close vicinity of the front. Note also there was considerable noise in the measurements, which resulted from the very nature of particle image velocimetry, which involved correlating the displacement over several successive images, as well as the substantial difference in the velocity amplitudes between the streamwise, normal, and cross-stream components.

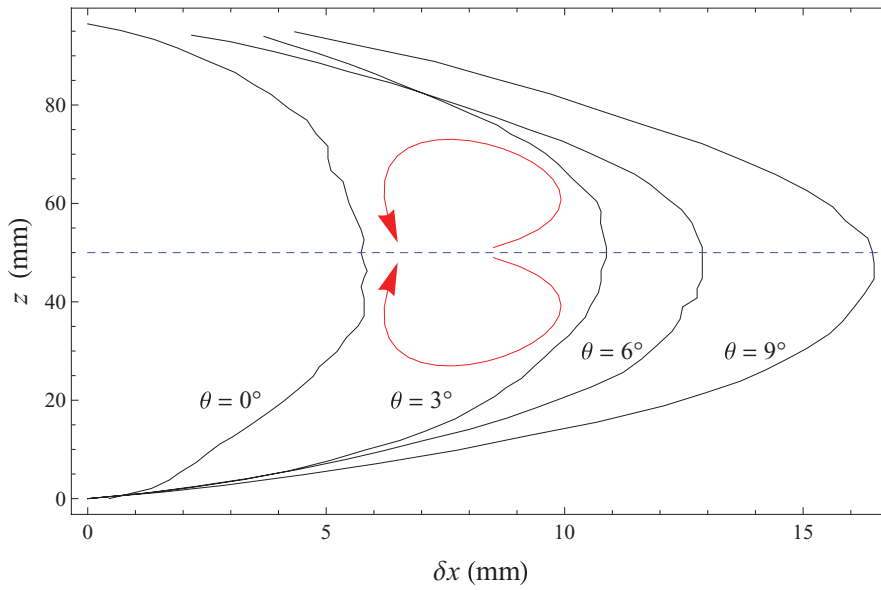


FIG. 6. Profiles of the contact lines seen from above for runs (a), (c)–(e) corresponding to slopes $\theta = 0^\circ$, 3° , 6° , and 9° , respectively. The postulated pair of counter-rotating vortices is also reported. The dashed line is the centerline. Distance x has been adapted to give the shape the same origin at the bottom left corner. Note that the width to length ratio is 6.66, so that the contact lines were blunter than they might appear.

Figure 7(a) plot can be usefully compared with Fig. 4(c) corresponding to the same inclination, but with a mass of 6 kg. Clearly, the agreement was much better with the lowest mass since the deviations between the observed and theoretical profiles were seen only near the contact line ($x - x_f \geq -2$ mm). This supports our earlier statement: the discrepancy between lubrication theory and experimental was likely to originate from the development of inertial effects, which started being significant for Reynolds numbers in excess of 10. This is confirmed by run (g), which pertained to

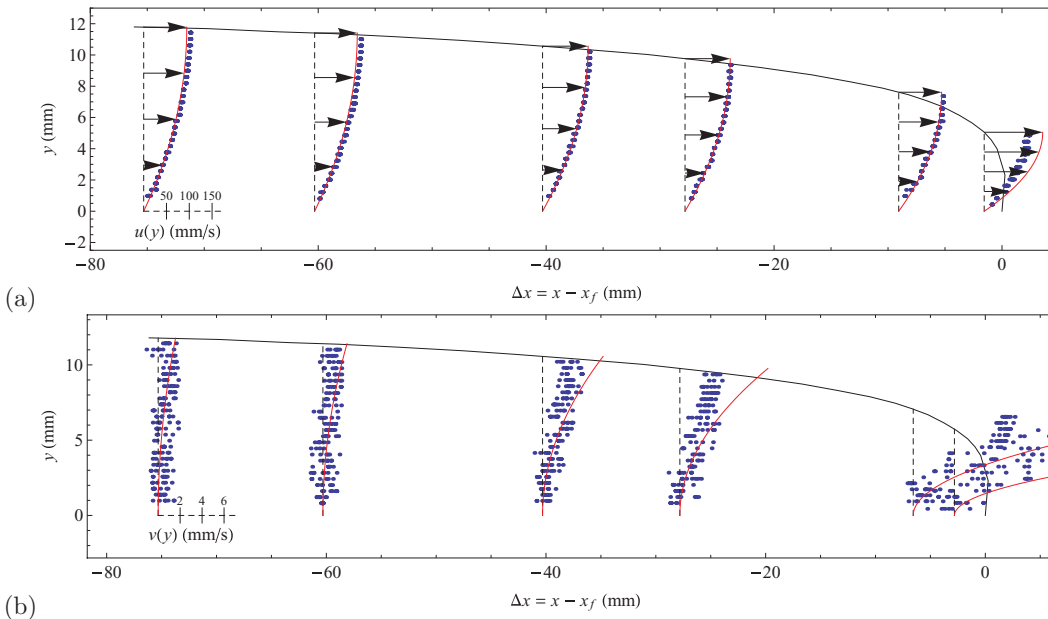


FIG. 7. (a) Streamwise velocity profiles for $\theta = 6^\circ$ [run (f)]. Initial mass released: 3 kg. Same caption as for Fig. 4. (b) Normal velocity profiles. The solid line is the theoretical velocity profile (4).

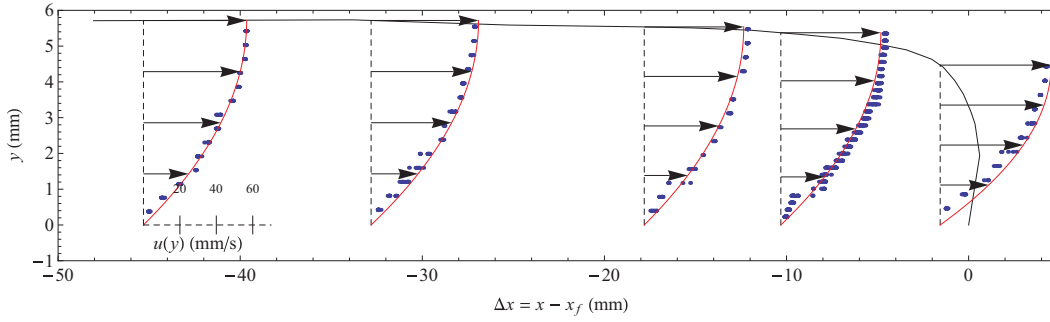


FIG. 8. Velocity profiles for $\theta = 25^\circ$ [run (g)]. Initial mass released: 1 kg. Same caption as for Fig. 4.

a steep slope ($\theta = 25^\circ$) but with a very low mass (1 kg instead of 3 or 6 kg). In spite of the steep slope, the flow was sufficiently shallow for the Reynolds number not to exceed 0.3 (see Table I) in the body. As shown by Fig. 8, there was also good agreement between the observed and theoretical profiles for this run.

C. Viscosity influence

We tested Triton X100, which could be roughly regarded as a Newtonian fluid in spite of its shear thinning. Figure 9 shows the measured velocity profiles together with the theoretical profiles given by Eq. (3). At first look, agreement was partial and, as the flow Reynolds was quite high ($Re \sim 9$), this may be due to the development of inertial effects. Yet, if we assumed a power-law constitutive relation [see Eq. (11)], we obtained the following velocity profile:

$$u(x, y, t) = \frac{n}{n+1} \tilde{K}^{1/n} (h^{1+1/n} - (h-y)^{1+1/n}) \left(1 - \cot\theta \frac{\partial h}{\partial x}\right)^{1/n} \quad \text{with } \tilde{K} = \frac{\rho g \sin\theta}{\kappa} \quad (12)$$

that closely matched the observations. Deviations from the theoretical trend were seen only near the contact line.

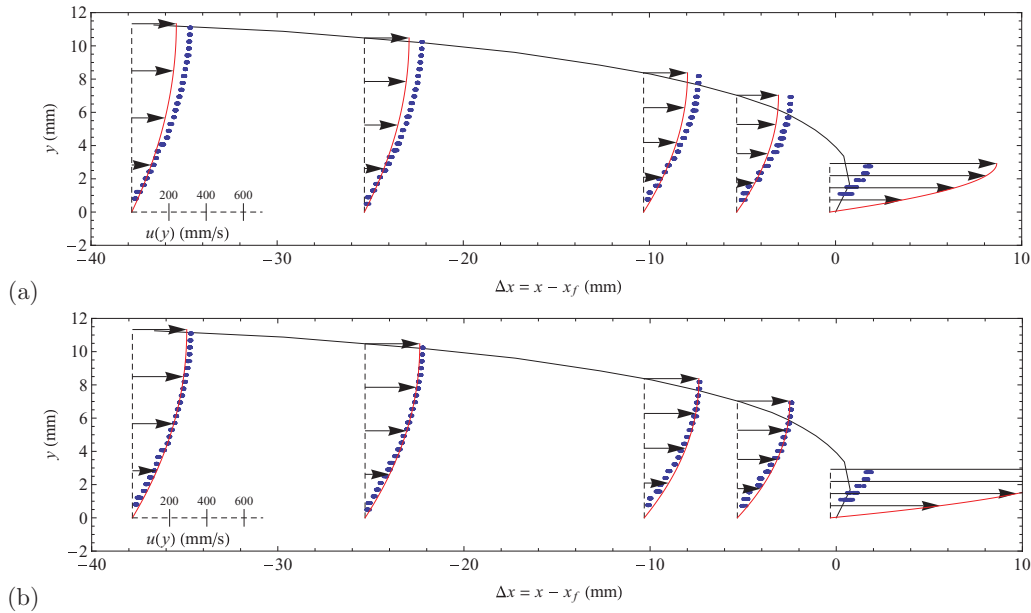


FIG. 9. Velocity profiles for the Triton sample [run (h)] ($\theta = 6^\circ$), initial mass released: 3 kg. (a) Theoretical profiles given by the Newtonian law (3). (b) Theoretical profiles given by the power law (12) with the parameters given by the rheometric data (11).

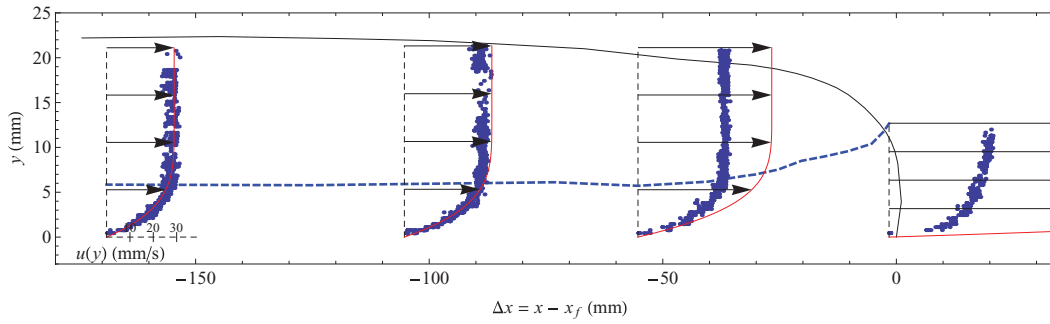


FIG. 10. Depth and velocity profiles for the Carbopol sample. Slope $\theta = 25^\circ$, initial mass released: 6 kg. The thick dashed line represents the pseudoyield surface. The dots represent the measurements, while the solid lines stand for the theoretical profiles provided by Eq. (10).

V. EXPERIMENTAL RESULTS FOR VISCOPLASTIC FLUIDS

Tests with viscoplastic materials turned out to be more difficult to carry out. While the overall pattern was similar to that observed for Newtonian fluids (i.e., fairly satisfactory agreement with lubrication theory, in particular sufficiently far from the contact line), we were faced with additional difficulties arising from slip occurrence and existence of a yield stress. Velocities data were also much more noisy (the Carbopol samples being translucent, image quality was less than with Newtonian fluids).

One way of reducing wall slip was to spread a thin layer of Carbopol prior to each experiment. Once dried, the layer was removed, but a thin coating film was likely to remain and change the surface state of the flume bottom. As shown by Walls *et al.*,³⁸ using hydrophilic or hydrophobic plates has significant influence on slip occurrence. Following the conclusions of Walls *et al.*,³⁸ we also think that the coating film reduced surface energy and thus slipping velocity to a significant degree but not completely as will be shown below.

Yield stress also had major effect on the avalanche dynamics. In particular, as shown by Eq. (10), bed inclination or flow depth must be sufficiently large for the flow to occur. At steep slope and/or for thick flows, the flow was rather fast and looked like the Newtonian flows described in Sec. IV, but at shallow slopes or for thinner flows, the flow was very slow and could come to a halt. In the following, we will give two typical examples of fast and slow flows.

Figure 10 shows the flow depth profile and velocity profiles for a 6-kg mass down a slope of 25° ; the position of the pseudoyield surface $y = Y_0(x, t)$ is also reported. Figure 11 provides more

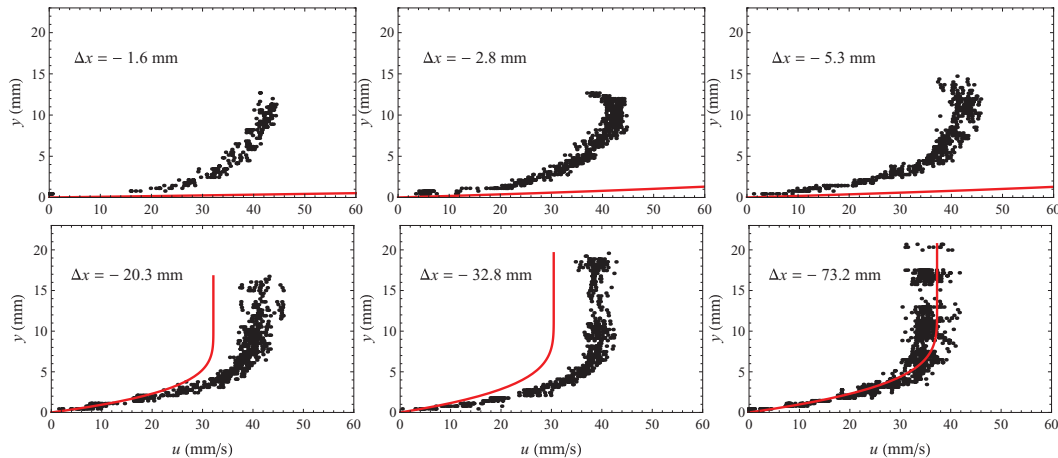


FIG. 11. Velocity profiles taken at different positions. Flume inclination 25° .

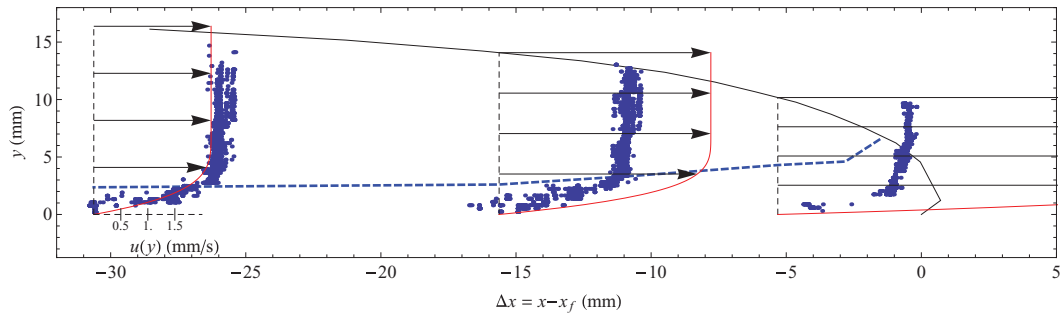


FIG. 12. Depth and velocity profiles for the Carbopol sample. Slope $\theta = 15^\circ$, initial mass released: 6 kg. The thick dashed line represents the pseudoyield surface. Same caption as for Fig. 10.

details on the changes in the velocity profile when one goes away from the front. For the body ($\Delta x < -100$ mm), there was good agreement between experiment and lubrication theory: both the velocity profile and position of the pseudoyield surface were properly predicted. When one approached the leading edge, deviations from the theoretical profile were conspicuous, but the position of the pseudoyield surface predicted by theory closely matched the observations. Near the contact line ($\Delta x \sim -1.6$ mm), the velocity profile took a parabolic shape that differed from the two-layer structure predicted by Eq. (10): consistently with Piau's statement,¹³ the plug region subsided and the entire depth was sheared. As the velocity data were noised, it was difficult to precisely determine where the plug region arose. For $-2 \leq \Delta x \leq -15$ mm, there was a slow transition from a parabolic shape to a two-layer structure.

Figure 12 provides an example of creeping (slow) flow. The flow configuration was the same as above except that the flume inclination was decreased to 15° . A noticeable consequence was the drop in the velocity magnitude: the maximum velocity did not exceed 2 mm/s whereas it exceeded 30 mm/s for $\theta = 25^\circ$. Four other features are also remarkable. First, the flow depth profile was markedly different, with a thinner, acuter leading edge whereas at steeper slopes, the tip region took the appearance of a blunt nose. Second, slipping was observed within the leading edge: as shown by Fig. 13, the slip velocity was approximately 1.8 mm/s, a value slightly lower than the free surface velocity (2.3 mm/s). Third, while the two-layer structure was obvious far away from the contact line, the shape of the velocity profile within the tip region ($\Delta x > -5$ mm) was more difficult to interpret: in addition to the slip component, there seemed to be slight but continuous shearing ($\dot{\gamma} \sim 5 \times 10^{-2} \text{ s}^{-1}$) across the depth. Fourth, the velocity of the free surface seemed to stay constant: far from the contact line (at $\Delta x = -30.6$ mm), it reached 23 ± 3 mm/s while in the vicinity of the contact line (at $\Delta x = -0.3$ mm), it was 24 ± 1 mm/s. This may indicate that the free surface was frozen, i.e., in a fully plastic state. The main difference between the body and the tip region lay in the collapse of the sheared layer, which reduced to a lean layer (thickness 0.2 mm).

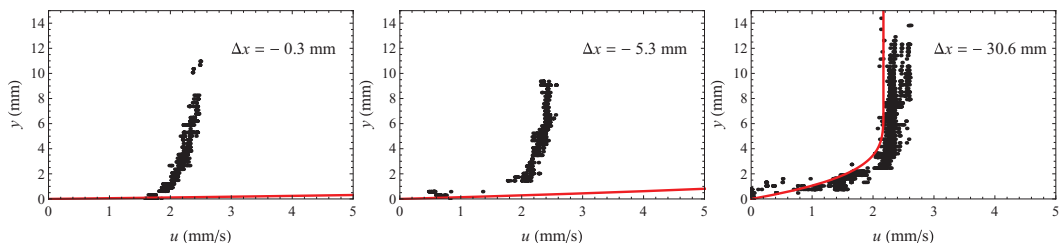


FIG. 13. Velocity profiles taken at different positions. Flume inclination 15° .

VI. CONCLUSIONS

As far as we are aware, this paper is the first report on velocity measurements within the head of fluid avalanches far from the sidewalls. We compared the velocity profiles predicted by lubrication theory to those measured experimentally within the head and body of fixed-volume flows over horizontal or down sloping beds under laminar flow conditions. Experiments were conducted for various flume inclinations and two kinds of fluids: Newtonian (glycerol, Triton X100) and viscoplastic (Carbopol ultrez 10).

For flows of Newtonian liquids at low Reynolds numbers, there was excellent agreement between lubrication theory and experiment except for the close vicinity of the contact line, where velocities were usually significantly overestimated by theory. At higher Reynolds numbers ($Re \sim 10$), lubrication theory slightly underestimated velocity (by approximately 10%). Interestingly enough, these velocity measurements shed new light on the discrepancy between theory and experiment as regards front propagation:

- In an earlier paper,²⁶ we assumed that the systematic deviation between the corresponding theoretical and experimental curves resulted from a delay due to the opening of the gate when we released the fluid down the flume. This deviation was more likely due the influence of three-dimensional structures that altered the velocity profiles along the centerline and, as shown in the Appendix, to sidewall friction. The explanation of the latter effect (occurrence of a pair of counter-rotating vortices) is speculative and deserves further work. We also observed that the higher the flow Reynolds number was, the larger the deviations between theoretical and experimental velocity profiles were.
- In lubrication theory, the front position equation (8) is derived by using an approximation that amounts to regarding the flow as a locally steady uniform flow. We showed that although this approximation did not hold true, in particular within the tip region owing to the curvature of the free surface (that makes the velocity field very different from the velocity distribution in a steady uniform flow), it provided reasonably accurate predictions of the front position to within 20%.

For viscoplastic flows, the experiments were more difficult to conduct. At sufficiently steep slopes (25°), there was satisfactory agreement between lubrication theory and experiment as long as the curvature of the free surface was not too marked. At shallower slopes (15°), agreement became poor. While the two-layer structure of the velocity profile predicted by theory was evident far from the contact line, the structure of the velocity field within the head was more complicated. In particular, significant wall slip was observed there.

ACKNOWLEDGMENTS

We are grateful for the financial support provided by the Swiss National Science Foundation under Grant No. 206021-133831, the competence center in Mobile Information and Communication Systems (a center supported by the Swiss National Science Foundation under Grant No. 5005-67322, MICS project), and the competence center in Environmental Sciences (TRAMM project). The second author of this paper, Gaël Epely-Chauvin, died accidentally during the writing of this paper, just before the revised version was submitted.

APPENDIX: EXACT AND APPROXIMATE SOLUTIONS TO THE DEPTH-AVERAGED EQUATIONS OF MOTION

1. Governing equations

In Sec II A, we omitted the effects of surface tension and inertia in the derivation of the governing equation (6). To appreciate the respective influence of surface tension and inertia, we can use the

following set of depth-averaged dimensionless equations reflecting mass conservation

$$\frac{\partial h}{\partial t} + \frac{\partial h\bar{u}}{\partial x} = 0, \quad (\text{A1})$$

and momentum conservation

$$\epsilon Re \left(\frac{\partial h\bar{u}}{\partial t} + \beta \frac{\partial h\bar{u}^2}{\partial x} \right) + \epsilon \cot \theta h \frac{\partial h}{\partial x} = h - \tau_b + \frac{\epsilon^3}{Ca} h \frac{\partial^3 h}{\partial x^3}. \quad (\text{A2})$$

These equations are derived from the Navier-Stokes equation using integral theory and a Kármán-Polhausen approach (see Craster and Matar² for an example of derivation). For the sake of simplicity, we have not used specific symbols to refer to dimensionless numbers, as in this Appendix, all variables are in dimensionless form. In the left-hand side of Eq. (A2), the first two terms represent the variations in the bulk momentum while the third term is the pressure gradient term. In the right-hand side of Eq. (A2), the first term represents the gravitational forces, the second term τ_b is the bottom shear stress, and the third contribution accounts for surface tension. In the momentum balance equation (A2), the advection term is weighted by the Boussinesq coefficient $\beta = \overline{u^2}/\bar{u}^2$, which reflects the effect of the shearing on the velocity distribution. By adopting the Kármán-Polhausen approach and assuming that the velocity profile is parabolic, we close the mass and momentum balance equations by setting

$$\tau_b = 3 \frac{\bar{u}}{h} \text{ and } \beta = \frac{5}{6}. \quad (\text{A3})$$

Equations (A1) and (A2) are parameterized by four dimensionless groups: the bed slope θ , the aspect ratio ϵ , the Reynolds number Re , and the capillary number Ca

$$\epsilon = \frac{H_*}{L_*}, Re = \frac{\rho H_* U_*}{\mu} \text{ and } Ca = \frac{\mu U_*}{\sigma}, \quad (\text{A4})$$

where $H_*, L_*, U_* = \rho g H_*^2 \sin \theta / \mu$ are typical scales of length, height, and velocity. In the present context, the typical orders of magnitude of these scales are: $H_* = 3$ cm, $L_* = 3$ m, $U_* = 50$ cm/s (estimates for $\mu = 1.1$ Pa s, $\theta = 3^\circ$, $\rho = 1260$ kg m⁻³, $\sigma = 60$ mN m⁻¹), yielding: $\epsilon = 10^{-2}$, $Re = 17$, and $Ca = 9$. This application shows that surface tension (which scales as $\epsilon^3 Ca^{-1} \sim 10^{-7}$) has negligible effects here, while inertia (which scales as $\epsilon Re \sim 2 \times 10^{-1}$) is sufficiently small to be neglected as a first approximation, but it may play a role, as discussed later. The pressure gradient (which scales as $\epsilon \cot \theta \sim 2 \times 10^{-1}$) is of the same order of magnitude as inertia for this numerical application. From this, we can simplify the mass and momentum balance equations (A1) and (A2)

$$\frac{\partial h}{\partial t} + \frac{\partial h\bar{u}}{\partial x} = 0, \quad (\text{A5})$$

$$\frac{\partial h\bar{u}}{\partial t} + \beta \frac{\partial h\bar{u}^2}{\partial x} + \frac{\cot \theta}{Re} h \frac{\partial h}{\partial x} = \frac{1}{\epsilon Re} \left(h - 3 \frac{\bar{u}}{h} \right). \quad (\text{A6})$$

To elucidate the respective role of the different contributions to the momentum balance equation, we solve Eqs. (A5) and (A6) numerically and analytically using asymptotic methods.

2. Characteristic form

The governing equations (A5) and (A6) can be cast into the characteristic form

$$\ell_{\pm} \frac{dh}{dt} + \frac{d\bar{u}}{dt} = \frac{1}{\epsilon Re} \left(1 - 3 \frac{\bar{u}}{h^2} \right) \text{ on } \frac{dx}{dt} = \lambda_{\pm}, \quad (\text{A7})$$

where

$$\ell_{\pm} = \frac{\bar{u}^2(\beta - 1) + \cot \theta Re^{-1} h}{h(\bar{u}(\beta - 1) \pm \sqrt{\beta \bar{u}^2(\beta - 1) + \cot \theta Re^{-1} h})}, \quad (\text{A8})$$

$$\lambda_{\pm} = \beta \bar{u} \pm \sqrt{\beta \bar{u}^2(\beta - 1) + \cot \theta Re^{-1} h}. \quad (\text{A9})$$

In the $x - t$ plane, the equations $dx/dt = \lambda_{\pm}$ form two (one-parameter) families of characteristic curves, along which the relation (A7) hold.³⁶ The wave front is the locus of points in the $x - t$ plane, for which the depth is zero and the velocity takes a finite nonzero value. In the absence of shearing ($\beta = 1$) and drag ($Re \rightarrow \infty$), the solution to the governing equations (A5) and (A6) is the Ritter solution (also called the dam break solution).^{36,39} In that case, both families of characteristic curves merge at the front; the wave front is then a characteristic curve. When $\beta > 1$ and drag is taken into account, the front wave is no longer a characteristic curve, but the envelope of the characteristics.⁴⁰ As the wave front is tangent to each characteristic when $h = 0$, it has the same slope dx/dt . When $h \rightarrow 0$, we have $\lambda_{\pm} = \gamma_2 \bar{u}_f + O(h)$ and $\ell_{\pm} = \bar{u}_f / (\gamma_1 h) + O(1)$ with $\gamma_1 = 1 + \sqrt{\beta/(\beta - 1)}$ and $\gamma_2 = \beta + \sqrt{\beta(\beta - 1)}$ and where $\bar{u}_f(t)$ denotes the front velocity. In the limit of vanishing flow depths and for $\beta > 1$, we have $\ell_{\pm} dh + d\bar{u} \approx \bar{u}_f^{1-\gamma_1} d(h\bar{u}_f^{\gamma_1}) / (\gamma_1 h)$, from which we deduce

$$\frac{\bar{u}_f^{1-\gamma_1}}{\gamma_1 h} d(h\bar{u}_f^{\gamma_1}) = -\frac{3}{\epsilon Re} \frac{\bar{u}_f dt}{h^2} + O(1) \text{ on } \frac{dx}{dt} = \gamma_2 \bar{u}_f + O(h). \quad (\text{A10})$$

After integration, we find that close to the front $x = x_f$, the flow depth varies as

$$h \approx \left(\frac{6}{\epsilon Re} \frac{\gamma_1}{\gamma_2 \bar{u}_f} (x_f - x) \right)^{1/2}, \quad (\text{A11})$$

a scaling that is in close agreement with earlier findings.^{7,39}

3. Numerical solution

A common strategy to solve the governing equations (A5) and (A6) is to use a fractional-step approach, which involves splitting the problem into two subproblems that can be solved independently and more easily:³⁶ first, solve the homogenous advection equation

$$\partial_t \mathbf{U} + \mathbf{A} \cdot \partial_x \mathbf{U} = 0, \text{ with } \mathbf{A} = \begin{bmatrix} 0 & 1 \\ \epsilon h \cot \theta - \beta \bar{u}^2 & 2\beta \bar{u} \end{bmatrix} \text{ and } \mathbf{U} = \begin{bmatrix} h \\ h\bar{u} \end{bmatrix}, \quad (\text{A12})$$

then solve the evolution equation

$$\partial_t \mathbf{U} = \mathbf{S}, \text{ with } \mathbf{S} = \frac{1}{\epsilon Re} \begin{bmatrix} 0 \\ h - 3 \frac{\bar{u}}{h} \end{bmatrix}. \quad (\text{A13})$$

For the first subproblem (A12), we used a high-resolution wave propagation algorithm developed by LeVeque.³⁶ This algorithm is a Godunov-type scheme that employs the solution to local Riemann problems. It is part of an open-source library called CLAWPACK. More specifically, we used an approximate Riemann solver developed by George,⁴¹ which provides a well-balanced scheme that preserves balanced steady states, properly captures shock waves and fronts over dry surfaces, and maintains depth non-negativity. For the second problem (A13), we used a backwards (implicit) Euler scheme.

Taking shearing into account, i.e., taking $\beta > 1$, leads to characteristic velocities in excess of the front velocity and in the absence of viscous drag, it is not possible to identify the location of the front, as the front is rejected to infinity, which has been already noticed when solving the dam break problem (with or without drag).^{39,42} For this reason, in the absence of expedient to fix this issue, we took $\beta = 1$ in the numerical simulations. Figure 14 shows a typical example of simulations with $\beta = 1$ for the initial boundary value problems that corresponded to runs (b)–(d) (same initial volume but different bed inclinations). The convergence of the numerical solutions to the similarity solution (A20) was rather fast: for $t \geq 0.5$, the simulated front position curves collapsed onto the curve given by Eq. (A20).

Numerically, it is possible to account for sidewall friction by utilizing the approximation of hydraulics radius used in hydraulics.^{43,44} Using the Darcy-Weisbach formula, Chow⁴³ showed that for open channel flows, the mean bottom shear stress can be expressed as

$$\tau_b = \frac{1}{8} f \rho \bar{u}^2, \quad (\text{A14})$$

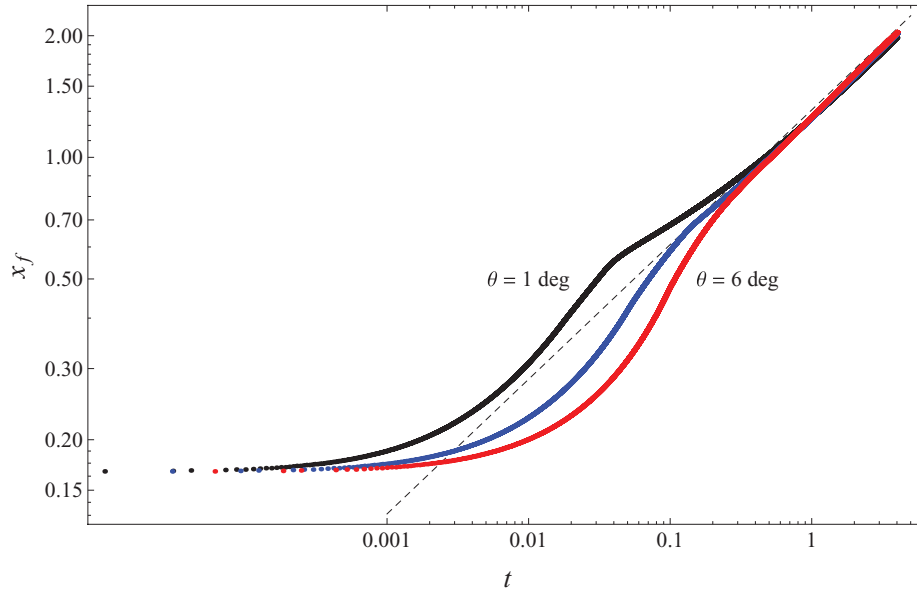


FIG. 14. Front position as a function time (dimensionless log-log plot). The flow conditions pertain to runs (b)–(d), i.e., for $\theta = 1^\circ, 3^\circ$, and 6° . The dashed line is the similarity solution (A20): $x_f = \xi_f t^{1/3}$. The dots represent the numerical data, which were obtained by solving the governing equations (A5) and (A6) with the same initial conditions as those imposed in our experiments. The scales were $L_* = 3$ m, $A_* = H_* L_* = 4.8 \times 10^{-2}$ m². $U_* = \rho g H_*^2 \sin \theta / \mu$.

where the Darcy-Weisbach friction factor f is expressed as $f = 24/Re_h$ with $Re_h = \rho \bar{u} R_h / \mu$ the generalized Reynolds number and $R_h = Wh/(W + 2h)$ the hydraulic radius (where W denotes the flume width). This amounts to weighting the bottom shear stress τ_b in the momentum balance equation (A2) with a correcting factor $1 + 2h/W$: $\tau_b = 3(1 + 2h/W)\bar{u}/h$. Figure 15 shows the comparison between experimental data and numerical simulations for runs (b)–(d), i.e., for a mass of 6 kg and slopes $\theta = 1^\circ, 3^\circ$, and 6° . We also report the similarity solution (A20). Using the empirical sidewall friction resulted in much better agreement with experimental data. This supports the idea that sidewall friction influenced the front dynamics in our narrow flume.

4. Analytical solution

We solve the following boundary value problem. We consider the flow generated by the removal of a lock gate, behind which a volume A of fluid is at rest. In the absence of surface tension, the governing equations are given by Eqs. (A5) and (A6). The equations are supplemented by an equation of mass conservation and a boundary condition at the front

$$\int_0^{x_f(t)} h(x, t) dx = A \text{ and } h(x_f) = 0. \quad (\text{A15})$$

Without losing generality, we can seek solutions in the form

$$h(x, t) = t^{-p} Z(\xi, t), \quad u(x, t) = t^{-q} V(\xi, t), \quad \text{and } \xi = \frac{x}{t^a}. \quad (\text{A16})$$

The continuity equation (A5) yields

$$(pZ + a\xi \partial_\xi Z) t^{a+q-1} = t^{a+q} \partial_t Z + \partial_\xi (ZV) \quad (\text{A17})$$

while the momentum balance equation (A6) leads to

$$\frac{1}{\epsilon Re} \left(1 - 3t^{q-2p} \frac{V}{Z^2} \right) t^{a+2q} + (qV + a\xi \partial_\xi V) t^{a+q-1} = t^{q-a} \partial_t V + V \partial_\xi V + \frac{\cot \theta}{Re} t^{2q-p} \partial_\xi Z. \quad (\text{A18})$$

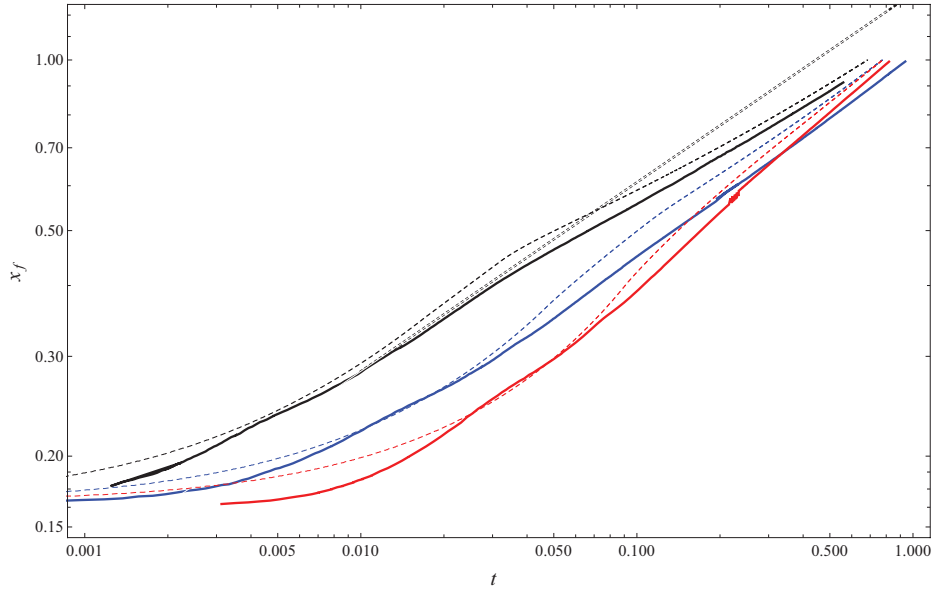


FIG. 15. Front position as a function time (dimensionless log-log plot) when sidewall friction is taken into account. The flow conditions pertain to runs (b)–(d), i.e., for $\theta = 1^\circ, 3^\circ$, and 6° . The dotted line is the similarity solution (A20): $x_f = \xi_f t^{1/3}$. The dashed lines stand for the numerical simulations while the solid lines represent the experimental data.

The outer solution is obtained by taking the limit $\epsilon Re \rightarrow 0$ and posing $Z(\xi, t) = Z_0(\xi) + t^{\alpha_1} Z_1(\xi) + \dots$ and $V(\xi, t) = V_0(\xi) + t^{\beta_1} V_1(\xi) + \dots$. We have $a = p$, $q = 2p$, and $a + q = 1$, which yields: $a = p = 1/3$ and $q = 2/3$. To leading order, we get

$$V_0 = \frac{1}{3} Z_0^2 \text{ and } Z_0 = \sqrt{\xi}. \quad (\text{A19})$$

The front position is determined using mass conservation (A15)

$$\xi_f = \left(\frac{3}{2} A \right)^{2/3}. \quad (\text{A20})$$

The depth profile and front position are the same as those calculated by Hunt⁷ using the shallow-flow (Saint-Venant) equations and Huppert¹⁷ from the Navier-Stokes equations. Since the flow depth does not drop to zero, we expect a boundary layer to occur at the front, where it is no longer possible to neglect the curvature of the free surface and its effect on pressure gradient in the momentum balance equation (A6).

To magnify what is occurring within this boundary layer, we now use the following change of variable: $\xi = \xi_f + \delta t^d \eta$, where δ is a free parameter and $d < 0$ a constant. From Eq. (A18), we see that at sufficiently long times (for $t \gg Retan\theta$), the pressure gradient term $\partial_\xi Z$ is much larger than the convection term $V \partial_\xi V$. The dominant balance is then between the pressure gradient term and the source term (gravitational force and viscous drag). We then deduce that $d = -2/3$ and $\delta = \epsilon \cot \theta$. Using the expansions $Z(\xi, t) = \hat{Z}_0(\xi) + t^{\gamma_1} \hat{Z}_1(\xi) + \dots$ and $V(\xi, t) = \hat{V}_0(\xi) + t^{\delta_1} \hat{V}_1(\xi) + \dots$ (with γ_i and δ_i constants), we deduce that to leading order, the balance and momentum balance equations are

$$\partial_\eta (\hat{Z}_0 (3 \hat{V}_0 - \xi_f)) = 0 \text{ and } 1 - 3 \frac{\hat{V}_0}{\hat{Z}_0^2} = \partial_\eta \hat{Z}_0, \quad (\text{A21})$$

subject to the boundary conditions when $\eta \rightarrow -\infty$

$$\hat{Z}_0 \rightarrow Z_f = \sqrt{\xi_f} \text{ and } \hat{V}_0 \rightarrow \xi_f/3. \quad (\text{A22})$$

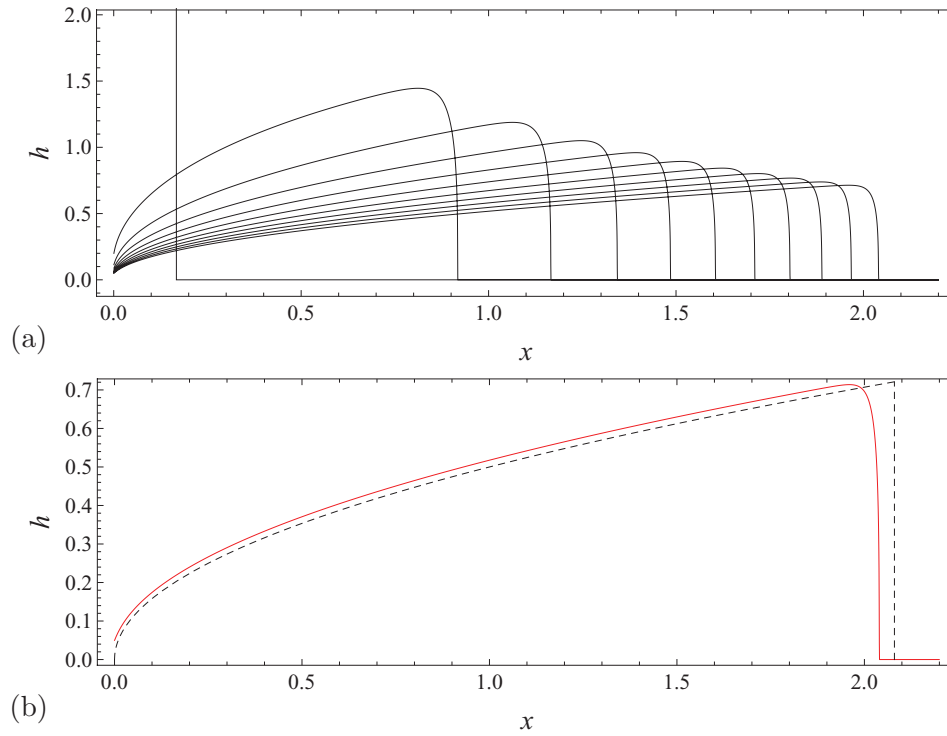


FIG. 16. Flow depth profiles for flow conditions pertaining to run (d), i.e., for a slope $\theta = 6^\circ$. (a) Time evolution of the depth profiles $h(x, t)$ for times $t = 0$ to $t = 4$ by time increment of 0.4. (b) Depth profile at time $t = 4$: comparison between the numerical solution (solid line) and analytical solution (A19) (dashed line).

The velocity field is constant while the depth profile is given by the implicit solution to

$$\hat{Z}_0 - Z_f \tanh^{(-1)} \frac{\hat{Z}_0}{Z_f} = \eta - \eta_f, \quad (\text{A23})$$

where η_f is a constant of integration, which can be determined by assuming that mass is merely distributed within the boundary layer with no creation or loss. We find that $\eta_f = (\ln 2 - 1/2)\sqrt{\xi_f}$. Returning to the initial variables, we have found that the front position is given by

$$x_f = \left(\frac{9}{4}A^2t\right)^{1/3} + (\ln 2 - 1/2) \left(\frac{3}{2}A\right)^{1/3} t^{-1/3} \epsilon \cot \theta. \quad (\text{A24})$$

The flow depth is the composite of the inner and outer solutions (A23) and (A19). Contrary to the outer solution, the inner solution slightly differs from the one worked out by Hunt,⁷ who assumed no time dependence of the boundary layer thickness; the shape is identical even though the mathematical expressions may look different. Note that the correction brought by the inner solution to the front position is low because of the $\epsilon t^{-1/3}$ dependence: quickly after the collapse, the similarity solution provides a reasonable approximation of the solution to the initial boundary value problem. Figure 16 shows the evolution of the flow depth profiles for the simulation of run (d). As seen in Fig. 16(a), the depth profile rapidly conforms to the parabolic shape given by Eq. (A19) and the thickness of the frontal boundary layer decreases rapidly as the mass spreads along the flume. Figure 16(b) is a close-up view of the depth profile at time $t = 4$, which compares the similarity solution (A19) with the computed profile.

¹ S. J. Weinstein and K. J. Ruschak, "Coating flows," *Annu. Rev. Fluid Mech.* **36**, 29–53 (2004).

² R. V. Craster and O. K. Matar, "Dynamics and stability of thin liquid films," *Rev. Mod. Phys.* **81**, 1131–1198 (2009).

³ P. Perona, "Bostwick degree and rheological properties: An up-to-date viewpoint," *Appl. Rheol.* **15**, 218–229 (2005).

- ⁴J. M. Piau and K. Debiane, "Consistometers rheometry of power-law viscous fluids," *J. Non-Newtonian Fluid Mech.* **127**, 213–224 (2005).
- ⁵N. J. Balmforth, R. V. Craster, P. Perona, A. C. Rust, and R. Sassi, "Viscoplastic dam breaks and the Bostwick consistometer," *J. Non-Newtonian Fluid Mech.* **142**, 63–78 (2007).
- ⁶T. R. H. Davies, "Debris-flow surges - Experimental simulation," *J. Hydrol. (NZ)* **29**, 18–46 (1990).
- ⁷B. Hunt, "Newtonian fluid mechanics treatment of debris flows and avalanches," *J. Hydraul. Eng.* **120**, 1350–1363 (1994).
- ⁸R. W. Griffiths, "The dynamics of lava flows," *Annu. Rev. Fluid Mech.* **32**, 477–518 (2000).
- ⁹C. Ancey, "Plasticity and geophysical flows: A review," *J. Non-Newtonian Fluid Mech.* **142**, 4–35 (2007).
- ¹⁰C. Ancey, "Gravity flow on steep slope," in *Buoyancy Driven Flows*, edited by E. Chassignet, and C. Cenedese (Cambridge University Press, New York, 2012).
- ¹¹J. E. Simpson, *Gravity Currents in the Environment and the Laboratory* (Cambridge University Press, Cambridge, 1997).
- ¹²M. Ungarisch, *An Introduction to Gravity Currents and Intrusions* (CRC, Boca Raton, 2009).
- ¹³J. M. Piau, "Flow of a yield stress fluid in a long domain. Application to flow on an inclined plane," *J. Rheol.* **40**, 711–723 (1996).
- ¹⁴X. Huang and M. H. Garcia, "A Herschel-Bulkley model for mud flow down a slope," *J. Fluid Mech.* **374**, 305–333 (1998).
- ¹⁵J. F. Gerbeau and B. Perthame, "Derivation of viscous Saint-Venant system for laminar shallow water: Numerical validation," *Discrete Contin. Dyn. Syst., Ser. B* **1**, 89–102 (2001).
- ¹⁶E. D. Fernández-Nieto, P. Noble, and J. P. Vila, "Shallow water equation for non-Newtonian fluids," *J. Non-Newtonian Fluid Mech.* **165**, 712–732 (2010).
- ¹⁷H. E. Huppert, "Flow and instability of a viscous current down a slope," *Nature (London)* **300**, 427–429 (1982).
- ¹⁸J. R. Lister, "Viscous flows down an inclined plane from point and line sources," *J. Fluid Mech.* **242**, 631–653 (1992).
- ¹⁹J. Gratton and F. Minotti, "Self-similar viscous gravity currents: Phase-plane formalism," *J. Fluid Mech.* **210**, 155–182 (1990).
- ²⁰K. F. Liu and C. C. Mei, "Approximate equations for the slow spreading of a thin sheet of Bingham plastic fluid," *Phys. Fluids A* **2**, 30–36 (1990).
- ²¹N. J. Balmforth and R. V. Craster, "A consistent thin-layer theory for Bingham plastics," *J. Non-Newtonian Fluid Mech.* **84**, 65–81 (1999).
- ²²J. S. Mathunjwa and A. J. Hogg, "Self-similar gravity currents in porous media: Linear stability of the Barrenblatt-Pattle solution revisited," *Eur. J. Mech. B. Fluids* **25**, 360–378 (2006).
- ²³N. J. Balmforth, R. V. Craster, A. C. Rust, and R. Sassi, "Viscoplastic flow over an inclined surface," *J. Non-Newtonian Fluid Mech.* **142**, 219–243 (2007).
- ²⁴G. P. Matson and A. J. Hogg, "Two-dimensional dam break flows of Herschel-Bulkley fluids: The approach to the arrested state," *J. Non-Newtonian Fluid Mech.* **142**, 79–94 (2007).
- ²⁵C. Ancey and S. Cochard, "The dam-break problem for Herschel-Bulkley fluids down steep flumes," *J. Non-Newtonian Fluid Mech.* **158**, 18–35 (2009).
- ²⁶C. Ancey, S. Cochard, and N. Andreini, "The dam-break problem for viscous fluids in the high-capillary-number limit," *J. Fluid Mech.* **624**, 1–22 (2009).
- ²⁷A. J. Hogg and G. P. Matson, "Slumps of viscoplastic fluids on slopes," *J. Non-Newtonian Fluid Mech.* **158**, 101–112 (2009).
- ²⁸N. Didden and T. Maxworthy, "The viscous spreading of plane and axisymmetric gravity currents," *J. Fluid Mech.* **121**, 27–42 (1982).
- ²⁹B. Nsom, K. Debiane, and J. M. Piau, "Bed slope effect on the dam break problem," *J. Hydraul. Res.* **38**, 459–464 (2000).
- ³⁰S. Cochard and C. Ancey, "Experimental investigation into the spreading of viscoplastic fluids on inclined planes," *J. Non-Newtonian Fluid Mech.* **158**, 73–84 (2009).
- ³¹C. C. Mei, "Nonlinear gravity waves in a thin sheet of viscous fluid," *J. Math. Phys.* **45**, 266–288 (1966).
- ³²H. E. Huppert, "The propagation of two-dimensional and axisymmetric viscous gravity currents over a rigid horizontal surface," *J. Fluid Mech.* **121**, 43–58 (1982).
- ³³F. K. Hansen and G. Rødsrud, "Surface tension by pendant drop: I. A fast standard instrument using computer image analysis," *J. Colloid Interface Sci.* **141**, 1–9 (1991).
- ³⁴M. Raffel, C. E. Willert, S. T. Wereley, and J. Kompenhans, *Particle Image Velocimetry* (Springer, Berlin, 2007).
- ³⁵J. K. Sveen, An Introduction to MatPIV v. 1.6.1, *Mechanics and Applied Mathematics Vol. 2* (Department of Mathematics, University of Oslo, August 2004).
- ³⁶R. J. LeVeque, *Finite Volume Methods for Hyperbolic Problems* (Cambridge University Press, Cambridge, 2002).
- ³⁷J. C. W. van Vroonhoven and W. J. J. Kuijpers, "A free-boundary problem for viscous fluid flow in injection moulding," *J. Eng. Math.* **24**, 151–165 (1990).
- ³⁸H. J. Walls, S. B. Caines, A. M. Sanchez, and S. A. Khan, "Yield stress and wall slip phenomena in colloidal silica gels," *J. Rheol.* **47**, 847–868 (2003).
- ³⁹A. J. Hogg and D. Pritchard, "The effects of hydraulic resistance on dam-break and other shallow inertial flows," *J. Fluid Mech.* **501**, 179–212 (2004).
- ⁴⁰L. Dressler, "Hydraulic resistance effect upon the dam-break functions," *J. Res. Natl. Bur. Stand.* **49**, 217–225 (1952).
- ⁴¹D. L. George, "Augmented Riemann solvers for the shallow water equations over variable topography with steady states and inundation," *J. Comput. Phys.* **227**, 3089–3113 (2008).
- ⁴²C. Ancey, S. Cochard, S. Wiederseiner, and M. Rentschler, "Front dynamics of supercritical non-Boussinesq gravity currents," *Water Resour. Res.* **42**, W08424, doi:10.1029/2005WR004593 (2006).
- ⁴³V. T. Chow, *Open-Channel Hydraulics* (McGraw-Hill, New York, 1959).
- ⁴⁴H. Chanson, *The Hydraulics of Open Channel Flow: An Introduction*, 2nd ed. (Heinemann, Amsterdam, 2004).